

Atypical homogeneous rheology of a high-entropy metallic glass challenges standard free volume models

Guanghui Xing(邢光辉), Bletry Marc, Mottelet Stephane, and Jichao Qiao(乔吉超)
Citation: Chin. Phys. B, 2025, 34 (**12**): 126402. DOI: 10.1088/1674-1056/adea5d
http://cpb.iphy.ac.cn; http://iopscience.iop.org/cpb

What follows is a list of articles you may be interested in

Molecular-dynamics simulations on the crystallization of Fe metallic glasses under alternating magnetic field

Yanxue Wu(吴言雪), Qiang-Qiang Pan(潘强强), Rui Ning(宁睿), and Hailong Peng(彭海龙)
Chin. Phys. B, 2025, 34 (**7**): 076402. DOI: 10.1088/1674-1056/adcb25

Unveiling the early stage evolution of local atomic structures in the crystallization process of a metallic glass

Lin Ma(马琳), Xiao-Dong Yang(杨晓东), Feng Yang(杨锋), Xin-Jia Zhou(周鑫嘉), and Zhen-Wei Wu(武振伟)
Chin. Phys. B, 2024, 33 (**3**): 036402. DOI: 10.1088/1674-1056/ad24d6

Effect of overheating-induced minor addition on Zr-based metallic glasses

Fu Yang(杨福), Zhenxing Bo(薄振兴), Yao Huang(黄瑶), Yutian Wang(王雨田), Boyang Sun(孙博阳), Zhen Lu(鲁振), Baoan Sun(孙保安), Yanhui Liu(柳延辉), Weihua Wang(汪卫华), and Mingxiang Pan(潘明祥)
Chin. Phys. B, 2024, 33 (**3**): 036401. DOI: 10.1088/1674-1056/ad1823

A group of ductile metallic glasses prepared by modifying local structure of icosahedral quasicrystals

Qi Qiao(乔琪), Ji Wang(王吉), Zhengqing Cai(蔡正清), Shidong Feng(冯士东), Zhenqiang Song(宋贞强), Benke Huo(霍本科), Zijing Li(李子敬), and Li-Min Wang(王利民)
Chin. Phys. B, 2023, 32 (**11**): 116401. DOI: 10.1088/1674-1056/ace823

Crystallization evolution and relaxation behavior of high entropy bulk metallic glasses using microalloying process

Danhong Li(李丹虹), Changyong Jiang(江昌勇), Hui Li(栗慧), and Mahander Pandey
Chin. Phys. B, 2021, 30 (**6**): 066401. DOI: 10.1088/1674-1056/abd92c

---

Atypical homogeneous rheology of a high-entropy metallic glass challenges standard free volume models

Guanghui Xing(邢光辉)[1], Bletry Marc[2,†], Mottelet Stephane[3], and Jichao Qiao(乔吉超)[1]

[1] *School of Mechanics and Transportation Engineering, Northwestern Polytechnical University, Xi'an* 710072, *China*
[2] *PCM2E EA* 6299, *Université de Tours, Parc de Grandmont, Tours* 37200, *France*
[3] *TIMR (Integrated Transformations of Renewable Matter), Université de Technologie de Compiègne, ESCOM, Centre de Recherches Royallieu, Compiègne* 60203, *France*

(Received 19 May 2025; revised manuscript received 20 June 2025; accepted manuscript online 1 July 2025)

Metallic glasses (MGs) exhibit exceptional mechanical properties, but their application is often limited by brittleness. At elevated temperatures near the glass transition (T_g), they undergo homogeneous viscoplastic deformation, a regime commonly described using free volume (FV) theory. Despite its prevalence, the quantitative accuracy and applicability of FV models, particularly for transient behaviors, remain under investigation. This study examines the homogeneous rheology of a LaCeYNiAl high-entropy MG (HEMG) between 475 K and 490 K, and critically assesses the relevance of two prominent FV model formulations. Experimental characterization includes dynamic mechanical analysis and uniaxial tensile tests across various strain rates. The tensile data are subsequently analyzed using two elasto-viscoplastic constitutive frameworks incorporating distinct FV evolution kinetics: Spaepen's original formulation (model 1), and the bimolecular annihilation kinetics proposed by Van den Beukel/Sietsma (model 2). Our analysis reveals that model 1, when applied to steady-state flow, yields physically inconsistent negative parameters, calling its validity for homogeneous deformation into question. Model 2 demonstrates better qualitative agreement with the experimental stress–strain curves but still fails to accurately reproduce the stress overshoot features. Moreover, fitting model 2 requires unphysically low Young's modulus values and produces unusual negative apparent activation energies for key kinetic parameters, suggesting limitations in the model structure (e.g., neglecting explicit viscoelasticity) or possibly unique behavior in HEMGs. These findings highlight significant shortcomings of standard FV models in quantitatively capturing the homogeneous deformation of this HEMG, particularly its transient characteristics, and underscore the need for more refined constitutive descriptions.

Keywords: high entropy metallic glasses, rheology, constitutive modeling, free-volume theory

PACS: 64.70.pe, 66.20.Cy, 62.20.–x, 02.30.Hq

DOI: 10.1088/1674-1056/adea5d **CSTR:** 32038.14.CPB.adea5d

1. Introduction

Metallic glasses (MGs) have garnered significant attention due to their unique amorphous structure and exceptional mechanical properties, such as high strength, large elastic limits, and excellent corrosion resistance.[1–6] However, their pronounced brittleness at room temperature, attributed to rapid shear-band instability and propagation, severely limits their practical applications.[7] At elevated temperatures, particularly near the glass transition temperature, their complex viscoplastic behavior, stress-overshoot phenomena, and structural relaxation present significant challenges for theoretical modeling and practical utilization.[8] Notably, MGs exhibit nonlinear rheological characteristics in the homogeneous deformation regime at high temperatures, which are closely linked to the evolution of free volume.[3]

The free volume theory, initially proposed by Cohen and Turnbull, has been widely used to describe the transport properties and deformation behavior of both liquid and glassy materials.[9,10] Spaepen extended this concept to MG plasticity, establishing an exponential relationship between the concentration of flow defects c_f and the free volume v_f, along with a stress–strain-rate-dependent constitutive equation.[11,12] Van den Beukel and Sietsma further introduced both dynamic and static free-volume evolution mechanisms, proposing a bimolecular annihilation equation to capture the influence of strain rate and temperature on structural relaxation.[13–15] Bletry *et al.* experimentally validated the predictive capability of the free volume model for steady-state flow stress in Zr-based MGs under high-temperature compression and revealed the cooperative motion of activation volumes involving approximately 10–20 atoms per shear event.[16,17] Gao *et al.* developed a thermoviscoplastic constitutive law based on free volume theory to analyze thermo-mechanical instabilities during heterogeneous deformation of amorphous alloys, constructing deformation mechanism maps consistent with experimental observations.[18] Anand and Su extended free volume theory into a three-dimensional, thermodynamically consistent finite-deformation continuum framework by incorporating additional coupling variables.[19] Zhang *et al.* formulated a plasticity constitutive equation integrating free volume theory

†Corresponding author. E-mail: mbl@univ-tours.fr

© 2025 Chinese Physical Society and IOP Publishing Ltd. All rights, including for text and data mining, AI training, and similar technologies, are reserved.

with brittle solid fracture theory to describe plastic flow in bulk MGs.[20] Zhu *et al.*[21] established a continuum model based on thermodynamic principles and free-volume concentration gradients, successfully reproducing shear-band instability and shear dilatation phenomena. Their model predicts a critical creep power-law transition governed by two distinct diffusion mechanisms activated by thermal and strain energy gradients.

Over the past decade, studies have further elucidated the intricate influence of free-volume distribution on mechanical properties. Stolpe *et al.*[22] investigated free-volume evolution in Zr-based MGs during cold rolling, revealing a linear relationship between total free volume and shear-band density. Lee *et al.*[23] extracted free-volume model parameters for Zr-based thin-film MGs through molecular dynamics simulations and finite-element analysis, validating their role in shear-band localization. Huang *et al.*[24] employed nano-CT imaging to analyze the microstructure of shear bands in Pd-based MGs and used free-volume-based finite-element simulations to examine their formation mechanisms. Chen *et al.*[25] utilized in situ high-pressure synchrotron x-ray diffraction to reveal large-scale homogeneous mixing of liquid and solid regions, proposing a "nested fractal network" model that provides experimental support for free volume theory and enhances its conceptual framework.

As a fundamental theoretical framework for understanding the mechanical behavior of amorphous materials, free volume theory establishes a crucial link between atomic-scale free-volume evolution and macroscopic mechanical responses, offering valuable insights into microscopic deformation mechanisms and mechanical-property optimization of MGs. However, free volume theory still has limitations, such as difficulties in capturing transient phenomena (e.g., stress overshoot) and uncertainties in key parameters (e.g., equilibrium free-volume concentration and dynamic evolution parameters).

Incidentally, a connection should exist between "flow defects" and "microstructural heterogeneities", which essentially represent different manifestations of the same physical phenomenon — a consensus supported by recent experimental studies and theoretical models. As a typical disordered solid, metallic glass lacks the long-range periodicity of crystalline materials but exhibits pronounced multiscale structural heterogeneity. This heterogeneity manifests directly as "flow defects" during deformation — localized regions where plastic flow preferentially occurs. Using amplitude-modulated dynamic atomic force microscopy (AM-AFM) and angstrom-scale coherent electron diffraction, Zhu *et al.*[26] directly observed spatial heterogeneity in MGs, identifying two types of nanoregions: high-density regions rich in icosahedral ordered structures, and low-density regions containing geometrically unstable crystal-like structures. Such fluctuations in density and structural order serve as the structural carriers of flow defects. Ge *et al.*[27] controlled the uniform plastic flow of $Zr_{50}Cu_{40}Al_{10}$ metallic glass via mandrel winding, combined with synchrotron small-angle/wide-angle x-ray scattering (SAXS/WAXS). They experimentally identified a characteristic scale of flow-induced structural heterogeneity of 2.5–3.5 nm, consistent with the size of "rheological units" predicted by molecular dynamics simulations.[27] Through quantitative characterization via three-dimensional Fourier analysis, Duan *et al.*[28] showed a linear positive correlation above 0.93 between the uniform plastic deformation capacity of MGs after yielding and the intensity of nanoscale heterogeneity. This finding directly confirms that regulating structural heterogeneity is an effective approach to suppress shear-band instability and enhance macroscopic plasticity. Under external loading, these pre-existing structurally heterogeneous regions are preferentially activated as flow defects, triggering localized shear deformation that eventually evolves into macroscopically visible shear bands. Thus, "flow defects" essentially represent the dynamic manifestation of microstructural heterogeneity in MGs during plastic deformation.[21,29]

This study aims to investigate the mechanical behavior of LaCeYNiAl HEMG within the temperature range of 475–490 K through experimental and theoretical analyses, with a particular focus on assessing the applicability of free volume models in describing their viscoplastic deformation. Dynamic mechanical analysis (DMA) and tensile testing are employed to acquire experimental data, revealing characteristic relaxation peaks and viscoplastic features in stress–strain curves. Subsequently, we compare the predictive capabilities of two free-volume models by fitting experimental data and evaluating their effectiveness in describing both steady-state and transient behaviors. Special attention is given to the temperature dependence of key model parameters (e.g., activation volume, attempt frequency, and Young's modulus) and the limitations of these models in capturing stress overshoot and inelastic effects. The findings provide deeper insights into the deformation mechanisms of MGs and offer guidance for optimizing their performance under high-temperature conditions.

2. Method

2.1. Sample preparation

In this study, LaCeYNiAl[30,31] alloys were selected as model MGs. The master alloy ingots were synthesized via arc melting of high-purity elemental metals ($\geq$ 99.9%) under an argon atmosphere. To ensure chemical homogeneity, the melting process was repeated six times. Subsequently, metallic glass ribbons with an approximate thickness of 35 μm were fabricated using a single-roller melt-spinning technique under an argon environment. The glass transition temperature of the LaCeYNiAl high-entropy metallic glass (HEMG), measured by DSC at 10 K/min, is 478 K.

2.2. Mechanical testing

2.2.1. Dynamic mechanical analysis

The dynamic mechanical relaxation behavior of the metallic glass samples was characterized using a commercial dynamic mechanical analyzer (TA DMA 850). During testing, a sinusoidal stress was applied, and the resulting strain response was recorded. The storage modulus E' and loss modulus E'' were determined. The experiments were conducted in tensile mode with a heating rate of 3 K·min^{-1} and applied frequencies of 1 Hz, 2 Hz, 4 Hz, and 8 Hz.

The E' and E'' were calculated based on the viscoelastic response of materials under sinusoidal alternating stress or strain. By applying a sinusoidal excitation with frequency ω (e.g., $\sigma(t) = \sigma_0 \sin(\omega t)$), the resulting strain response $\varepsilon(t) = \varepsilon_0 \sin(\omega t + \delta)$ was measured, where δ denotes the phase difference between stress and strain. The storage modulus, characterizing the elastic energy storage capacity, is defined as $E' = (\sigma_0/\varepsilon_0)\cos\delta$, reflecting the in-phase elastic deformation component. The loss modulus, representing energy dissipation, is given by $E'' = (\sigma_0/\varepsilon_0)\sin\delta$, corresponding to the out-of-phase viscous component. Both can be unified through the complex modulus $E^* = E' + \mathrm{i}E''$ (where i is the imaginary unit). Experimentally, DMA devices directly record the phase angle δ and the stress–strain amplitude ratio to compute E' and E''. Their temperature-dependent variations characterize relaxation processes in the glass transition region (e.g., decreasing E' indicates stiffness attenuation, while the E'' peak corresponds to maximum energy dissipation).

2.2.2. Uniaxial tensile testing

Uniaxial tensile tests were conducted using the strain-rate mode of the TA DMA 850 system. After stabilizing the sample at the target temperature for a designated period, a prescribed tensile strain rate was applied to the ribbon specimen. The stress evolution over time was recorded at various strain levels. The testing temperature range was set between 475 and 490 K, corresponding to temperatures close to T_g and ensuring homogeneous deformation under the applied loading conditions.

3. Experimental results

3.1. DMA

Isochronous DMA results are presented in Fig. 1. A typical α-relaxation peak appears around 500 K (depending on frequency), along with a distinct β-relaxation peak near 390 K. The peak temperatures of the α relaxation measured at different driving frequencies are plotted in the inset of Fig. 1 and fitted using the Vogel–Fulcher–Tammann (VFT) equation,[32,33] which reads

$$f_\alpha = f_{\alpha,0} \exp\left(-\frac{D^* T_0}{T - T_0}\right), \tag{1}$$

where $f_{\alpha,0}$ is the pre-exponential factor, D is the kinetic fragility parameter describing deviations from Arrhenius behavior (glasses with large D are considered strong, whereas those with low D are fragile), and T_0 is the ideal glass transition temperature, lower than the experimental T_g.

In this study, we obtained $D^* = 3.357$ K and $T_0 = 436.98$ K. Such low D^* values are commonly observed in various MGs, including Au-, Ca-, and Ni-based compositions.[34]

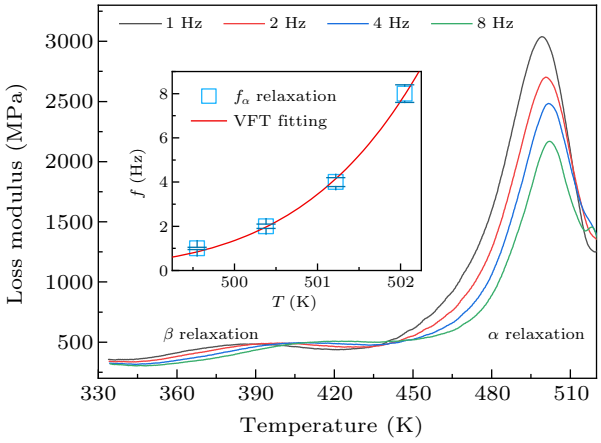


Fig. 1. Temperature dependence of the loss modulus of LaCeYNiAl MG at different driving frequencies (1 Hz, 2 Hz, 4 Hz, and 8 Hz). The heating rate is 3 K/min.

3.2. Tensile tests

Figure 2(a) presents the experimental stress–strain tensile curves obtained between 475 K and 490 K (engineering strain rates $\dot{\varepsilon}_e$ are provided in the caption). Overall, the curves exhibit the characteristic viscoplastic behavior of MGs, including a pronounced decrease in flow stress with increasing temperature and the presence of stress overshoots. Slight stress oscillations appear in the final segment, where $\dot{\varepsilon}_e$ decreases from 1×10^{-3} s^{-1} to 10^{-4} s^{-1}.

Because the data were acquired in terms of engineering strain (ε_e) and engineering stress (σ_e), it is essential to convert them to true stress (σ_t), true strain (ε_t), and true strain rate ($\dot{\varepsilon}_t$) for quantitative analysis. Assuming isochoric deformation, the tensile relations are

$$\varepsilon_t = \ln(1+\varepsilon_e), \quad \dot{\varepsilon}_t = \frac{\dot{\varepsilon}_e}{1+\varepsilon_e}, \quad \sigma_t = \sigma_e(1+\varepsilon_e). \tag{2}$$

4. Hyperbolic sine analysis

A commonly used framework for analyzing the rheological response of MGs is the hyperbolic sine relation

$$\dot{\varepsilon} = \dot{\varepsilon}_0 \sinh\left(\frac{\sigma V}{2\sqrt{3} k_B T}\right), \tag{3}$$

where V is the activation volume, $\dot{\varepsilon}_0$ is a frequency factor, and the remaining symbols carry their usual meanings. This form was originally proposed for glasses by Kauzmann[35] and has since been adopted in various models, including those of Spaepen,[12] Argon,[36] and Zhu *et al.*[37]

When fitting the parameters, it is crucial that the stress–strain-rate pairs used correspond to states that are as isoconfigurational as possible. Therefore, when analyzing strain-rate jump tests, it is preferable to use the maximum stress overshoot values rather than the steady-state plateaus, which is the approach adopted here. In general, the strain rate follows a hyperbolic sine dependence on stress, consistent with the behavior usually observed in MGs.

The data points plotted in Fig. 2(b) show a consistent trend across all strain-rate jump measurements. These values were calculated using true stress and true strain rate; using engineering quantities instead leads to substantial deviations, typically doubling the apparent activation volume and reducing $\dot{\varepsilon}_0$ by roughly half compared with the true values.

The fitted parameters are summarized in Table 1. The activation volume V tends to increase with temperature, except at $T = 475$ K, where the premature failure of the sample at the highest strain rate likely affected the fitted values. The prefactor $\dot{\varepsilon}_0$ exhibits a consistent increase with temperature.

Table 1. Parameters of Eq. (3) fitted to experimental data (see Fig. 2(f)).

T (K)	$\dot{\varepsilon}_0$ (s^{-1})	V (Å^3)
475	3.64×10^{-5}	405
480	1.27×10^{-4}	338
485	2.35×10^{-4}	377
490	3.52×10^{-4}	457

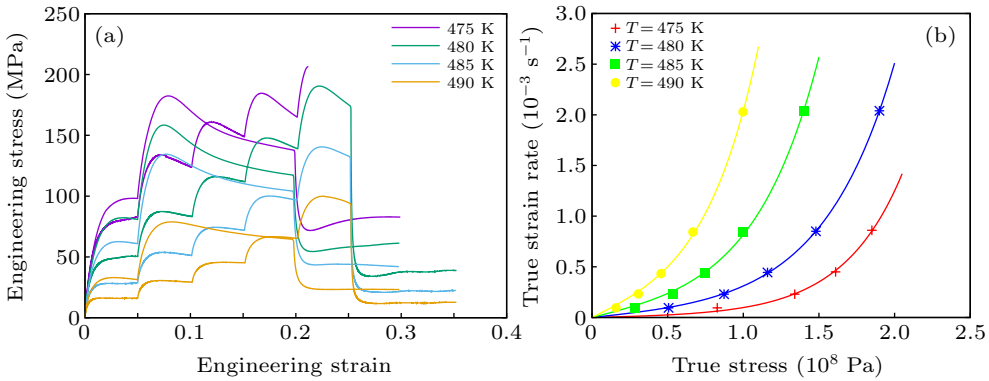


Fig. 2. (a) Tensile tests performed between 475 K and 490 K. The 6-sequence tests were conducted at $\dot{\varepsilon}_e = 10^{-4}$ s^{-1}, 2.5×10^{-4} s^{-1}, 5×10^{-4} s^{-1}, 1×10^{-3} s^{-1}, 2.5×10^{-3} s^{-1}, and back to 10^{-4} s^{-1}. The 3-sequence tests were conducted at $\dot{\varepsilon}_e = 2 \times 10^{-4}$ s^{-1}, 1×10^{-3} s^{-1}, and back to 2×10^{-4} s^{-1}. (b) Fit of Eq. (3) (lines) to the true stress and true strain rate data points.

The values of $\dot{\varepsilon}_0$ correspond to an activation energy of about 200 kJ/mol and a frequency factor of 6.4×10^{17} s^{-1}. These values are typical of those usually reported for MGs.

To go beyond such rheological analysis, one must consider a model richer than Eq. (3). Many models have been proposed to describe the mechanical behaviour of MGs. Among them, the long-standing free volume model — probably one of the most extensively studied frameworks in the experimental literature — is the focus of the next section.

5. Free volume modeling

5.1. Free volume model

The free volume model developed for liquids by Cohen and Turnbull[9,10] was initially adapted to MGs by Spaepen.[12] It includes a constitutive law for the relationship between stress and the strain-rate of the viscoplastic component, analogous to Eq. (3), which for uniaxial tests is written as

$$\dot{\varepsilon}_{vp} = c_f \dot{\varepsilon}_{0,c} \sinh\left(\frac{\sigma V}{2\sqrt{3}kT}\right), \tag{4}$$

where $c_f = \exp(-1/x)$ and $x = v_f/(\alpha v^*)$, with v_f the average free volume, v^* a critical free volume and α a geometrical factor that accounts for overlap between free-volume defects; $\dot{\varepsilon}_{0,c} = 2\nu_D \exp(-\Delta G^m/(kT))$ with ν_D the vibration frequency, ΔG^m an activation energy, and k and T having their usual meaning; V is the activation volume. This equation is common to all flavours of the free volume model — and even beyond, as the STZ theory of Argon[36] or the bond deficiency model[37] proposed by Zhu *et al.* lead to a similar relationship, as noted above.

The differences between these theories lie in the handling of c_f (or x). In particular, Spaepen's approach has generated several expressions to this end. In his original paper, he proposed[12]

$$\dot{x} = \frac{\nu_D}{\alpha} \exp\left(-\frac{\Delta G^m}{kT}\right) c_f \left\{ \frac{2kT}{\mu^* v^*} x^{-1} \times \left[\cosh\left(\frac{\sigma V}{2\sqrt{3}kT}\right) - 1\right] - \frac{1}{n_D} \right\}, \tag{5}$$

where $\mu^* = \frac{2}{3}\mu \frac{1+\nu}{1-\nu}$ with μ the shear modulus and ν Poisson's ratio, and n_D the number of diffusive jumps required to annihilate a flow defect. This model will hereafter be referred to as model 1.

Another formulation for the kinetic evolution of free volume (model 2) has been extensively studied by van den

Beukel, Siestma and collaborators using thermocalorimetry and tensile experiments performed in the homogeneous domain[13,38]

$$\dot{x} = a_x \dot{\varepsilon}_{\rm vp} - k_{\rm r} x^2 \left(\exp\left(-x^{-1}\right) - c_{\rm eq}\right), \tag{6}$$

where a_x is the coefficient of free-volume creation by strain, $k_{\rm r}$ is the structural relaxation constant, and $c_{\rm eq}$ is the equilibrium flow-defect concentration, provided by the VFT law

$$c_{\rm eq} = \exp\left(\frac{DT_0}{T - T_0}\right), \tag{7}$$

where D and T_0 are material parameters. When written for $\dot{c}_{\rm f}$, Eq. (6) represents a bimolecular annihilation equation that accounts for the linear increase of viscosity with time during structural relaxation.[11,38,39] To model creep, Heggen *et al.* used an equation somewhat similar to Eq. (6), but omitting the $c_{\rm eq}$ term, writing

$$\dot{x} = a_x \dot{\varepsilon}_{\rm vp} - k_{\rm r} x^2 \exp\left(-x^{-1}\right). \tag{8}$$

This last equation is only a special case of Eq. (6) and is valid far below $T_{\rm g}$, which is not our situation; thus it is not examined further.

To reproduce stress–strain curves obtained in uniaxial tests — whether in compression or tension — one needs to add at least one additional ingredient: the elastic component. In that case, the total strain-rate is written as

$$\dot{\varepsilon} = \dot{\varepsilon}_{\rm el} + \dot{\varepsilon}_{\rm vp} = \frac{\dot{\sigma}}{E} + c_{\rm f} \dot{\varepsilon}_{0,\rm c} \sinh\left(\frac{\sigma V}{2\sqrt{3} kT}\right), \tag{9}$$

where E is Young's modulus. This equation must then be combined with a formulation for $\dot{x}$, such as those introduced above, to model the experimental results. The combination of Eqs. (6) and (9) has been shown to provide satisfactory fits for several MGs deformed in the homogeneous domain[17,40] and is consistent with thermodynamic data.[41] The combination of Eq. (5) with one variation or another of Eq. (9) (possibly in tensorial form) has been used to model localisation phenomena[12,18,42–45] but — to the best of our knowledge — has never been employed to account for compression or tensile results obtained in the homogeneous domain.

5.2. Stationary states

When plateau stresses are reached, both models predict that the flow-defect concentration becomes constant ($c_{\rm f}^*$), corresponding to the stationary states of the $\dot{x}$ models.

5.2.1. Model 1

The first free-volume creation/annihilation model considered here, Eq. (5), leads to the explicit relation

$$c_{\rm f}^* = \exp\left(\frac{\frac{2kT}{\mu^* v^*}}{n_{\rm D}\left(1 - \cosh\left(\frac{\sigma V}{2\sqrt{3} kT}\right)\right)}\right). \tag{10}$$

However, a more convenient route is obtained by rewriting, from Eq. (4)

$$c_{\rm f}^* = \frac{\dot{\varepsilon}}{\dot{\varepsilon}_{0,\rm c} \sinh\left(\frac{\sigma V}{2\sqrt{3} kT}\right)}. \tag{11}$$

For clarity, we introduce the following notations:

(i) $B_1 = \dot{\varepsilon}_{0,\rm c}$.

(ii) $B_2 = V/(2\sqrt{3}kT)$.

(iii) $B_3 = \delta/A_v$, where $\delta = 1/n_{\rm D}$, $A_v = 2kT/(v^*\mu^*)$, and $\mu^* = \frac{2}{3}\mu\frac{1+\nu}{1-\nu}$.

All these parameters must be positive. By combining Eqs. (10) and (11), one obtains for each plateau stress/strain-rate pair $(\sigma_i, \dot{\varepsilon}_i)$

$$\frac{\dot{\varepsilon}_i}{B_1 \sinh(\sigma_i B_2)} - \exp\left(\frac{B_3}{1 - \cosh(\sigma_i B_2)}\right) = 0. \tag{12}$$

At least three such pairs may be used to determine the parameters through nonlinear least-squares fitting. This procedure is applied here using two data sets. The first set, taken from Ref. [46], corresponds to a Zr-based MG. The resulting fit and associated parameters are presented in Fig. 3 and Table 2. As can be seen, the parameter determination yields an acceptable fit quality; however, B_3 is found to be negative in both cases, which is physically meaningless.

The same type of negative B_3 values is also obtained using the results from the present study. The fitted parameters are listed in Table 3.

Table 2. The B_i's determined by nonlinear fitting from experimental data obtained from Ref. [46].

T (K)	B_1	B_2	B_3
613	1.6×10^{-6}	7.2×10^{-9}	-1.41
643	1.1×10^{-4}	8.9×10^{-9}	-6×10^{-2}

Table 3. The B_i's determined by nonlinear fitting from experimental data obtained in the present study.

T (K)	B_1	B_2	B_3
475	2.6×10^{-6}	4.6×10^{-8}	-20.3
480	4.3×10^{-6}	5.0×10^{-8}	-11.6
485	2.3×10^{-5}	4.1×10^{-8}	-1.6
490	6.7×10^{-5}	4.9×10^{-8}	-0.3

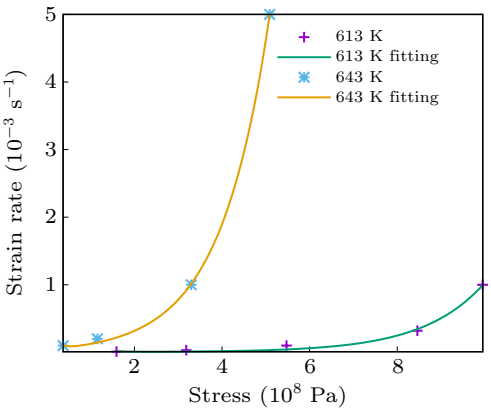


Fig. 3. Fitting of plateau stresses and strain rates — experimental data taken from Ref. [46].

This potential inability of model 1 to account for high-temperature rheological data casts doubt on its relevance as a viscoplastic framework for describing the high-temperature behaviour of MGs. In fact, when we attempted to fit an elasto-viscoplastic model based on model 1, using the numerical methods detailed in Subsection 5.3, we were unable to obtain acceptable agreement with the measured stress–strain curves. This further reinforces the view that model 1 is not well suited for reproducing strain-rate jump experiments or steady-state flow data. For this reason, we will not discuss this model further.

5.2.2. Model 2

In the case of Eq. (6) written in terms of $\dot{c}_\mathrm{f}$, one obtains the implicit relation

$$c_\mathrm{f}^* = c_\mathrm{eq} + \frac{a_x}{k_\mathrm{r}}\dot{\varepsilon}\ln^2(c_\mathrm{f}^*). \tag{13}$$

The combination of Eq. (13) with Eq. (5) has been shown to provide a satisfactory description of DSC measurements after deformation,[13,14] to rationalize mechanical data,[16] and to impose useful constraints on free parameters when modelling full stress–strain curves.[17]

5.3. Elasto-viscoplastic model

5.3.1. Numerical strategy

When adopting model 2, seven free parameters appear at a given temperature: E, $\dot{\varepsilon}_{0,\mathrm{c}}$, V, a_x, k_r, c_eq and c_i, the latter being the initial flow-defect concentration, which may vary from sample to sample. The parameter c_eq cannot be obtained from rheological data alone,[17] but according to free-volume theory it is given by the VFT law (see above)

$$c_\mathrm{eq} = \exp\left(-\frac{B}{T-T_0}\right). \tag{14}$$

To identify the remaining free parameters, we consider the following system of two ODEs derived from Eqs. (6) and (9)

$$\dot{x} = a_x\varepsilon_\mathrm{vp}(x,\sigma) - k_\mathrm{r}x^2\left(\exp(x^{-1}) - c_\mathrm{eq}\right), \tag{15}$$

$$\dot{\sigma} = E\left(\dot{\varepsilon} - \varepsilon_\mathrm{vp}(x,\sigma)\right), \tag{16}$$

where the auxiliary function $\varepsilon_\mathrm{vp}(x,\sigma)$ is defined by

$$\varepsilon_\mathrm{vp}(x,\sigma) = \exp(-x^{-1})\dot{\varepsilon}_{0,\mathrm{c}}\sinh\left(\frac{\sigma V}{2\sqrt{3}k_\mathrm{B}T}\right), \tag{17}$$

and the initial conditions read

$$\sigma(0) = 0, \tag{18}$$

$$x(0) = -(\ln c_i)^{-1}. \tag{19}$$

In what follows, we denote by $\sigma(t,\dot{\varepsilon};c_i,p)$ the solution of Eqs. (15)–(19), where $p = (E,\dot{\varepsilon}_{0,\mathrm{c}},V,a_x,k_\mathrm{r})$ is the vector of free parameters excluding c_i. The discrepancy between the model predictions and experimental stresses at discrete times for K experiments, given as pairs $(\sigma_j^k,t_j^k)_{j=1\ldots n_k}$ for $k = 1,\ldots,K$, is minimized in a least-squares sense by solving

$$RSS(\theta) = \sum_{k=1}^{K}\sum_{j=1}^{n_k}\left(\sigma_j^k - \sigma(t_j^k,\dot{\varepsilon}^k;c_i^k,p)\right)^2, \tag{20}$$

where $\dot{\varepsilon}^k$ and c_i^k denote the strain rate and the unknown initial defect concentration for experiment k. The values of $\sigma(t_j^k,\dot{\varepsilon}^k;c_i^k,p)$ are computed using the CVODE solver from the SUNDIALS suite,[47] and the minimization of $RSS(\theta)$ is performed using IPOPT.[48] Both solvers are available within the open-source numerical software Scilab,[49] which we therefore used for all computations.

The minimization procedure is carried out by supplying IPOPT with the exact partial derivatives of $RSS(\theta)$, computed using the complex-step technique,[50] yielding $\hat{\theta}$ defined by

$$\hat{\theta} = \arg\min_{\theta\in\Theta} RSS(\theta), \tag{21}$$

where the admissible set $\Theta \subset \mathbb{R}^{5+K}$ imposes bounds preventing unphysical parameter values.

The uncertainty in the fitted parameters is estimated using confidence intervals derived from the standard errors, which depend on the fitting standard error $\hat{s}$ defined by

$$\hat{s}^2 = \frac{RSS(\hat{\theta})}{N-5-K}, \tag{22}$$

where $N = \sum_{k=1}^{K} n_k$ and the denominator equals the degrees of freedom (number of scalar observations minus number of parameters). Parameter variances correspond to the diagonal entries of the inverse Fisher matrix[51]

$$F(\hat{\theta}) = \frac{1}{\hat{s}^2}\sum_{k=1}^{K}\sum_{j=1}^{n_k}\frac{\partial\sigma}{\partial\theta}(t_j^k,\dot{\varepsilon}^k;\hat{\theta})^\top\frac{\partial\sigma}{\partial\theta}(t_j^k,\dot{\varepsilon}^k;\hat{\theta}), \tag{23}$$

with sensitivities computed using the same complex-step technique. The rank of this matrix indicates parameter identifiability. With only one experiment, $F(\hat{\theta})$ becomes rank-deficient, meaning that certain parameters cannot be uniquely determined. When two experiments ($K = 2$) are used (see next section), the $1-\alpha$ confidence intervals of all parameters are given by

$$\hat{\theta}_i - t_{\alpha/2,N-5-K}\sqrt{V_{ii}} \le \theta_i \le \hat{\theta}_i + t_{\alpha/2,N-5-K}\sqrt{V_{ii}},$$
$$i = 1,2,\ldots,5+K, \tag{24}$$

where $V = F(\hat{\theta})^{-1}$ and $t_{\alpha/2,N-5-K}$ is the $1-\alpha/2$ quantile of the Student distribution with $N-5-K$ degrees of freedom. In the next section, the confidence intervals are reported as relative uncertainties.

5.3.2. Results

Figure 4 compares the model predictions with experimental data, and Table 4 provides the corresponding fitted parameter values. The parameter uncertainties vary: typically 0.6 % for E, 2 % for $\dot{\varepsilon}_{0,c}$, 0.3 % for V, and 2 % for a_x (except at $T = 490$ K, where it reaches 22 %), and about 6 % for k_r (with an exception at $T = 475$ K, where it reaches 39 %).

Table 4. Table of the fitted parameters at $T = 480$ K.

T (K)	E (GPa)	$\dot{\varepsilon}_{0,c}$ (s^{-1})	V (Å^3)	a_x	k_r (s^{-1})	c_{eq}
490	7.4	1.95×10^{8}	780	3.40×10^{-4}	3.64×10^{9}	9.60×10^{-13}
485	9.7	2.02×10^{9}	585	1.75×10^{-3}	2.42×10^{10}	5.38×10^{-14}
480	12.3	3.37×10^{10}	455	3.40×10^{-3}	5.50×10^{11}	1.54×10^{-15}
475	11.5	1.28×10^{11}	420	7.30×10^{-3}	4.70×10^{12}	1.74×10^{-17}

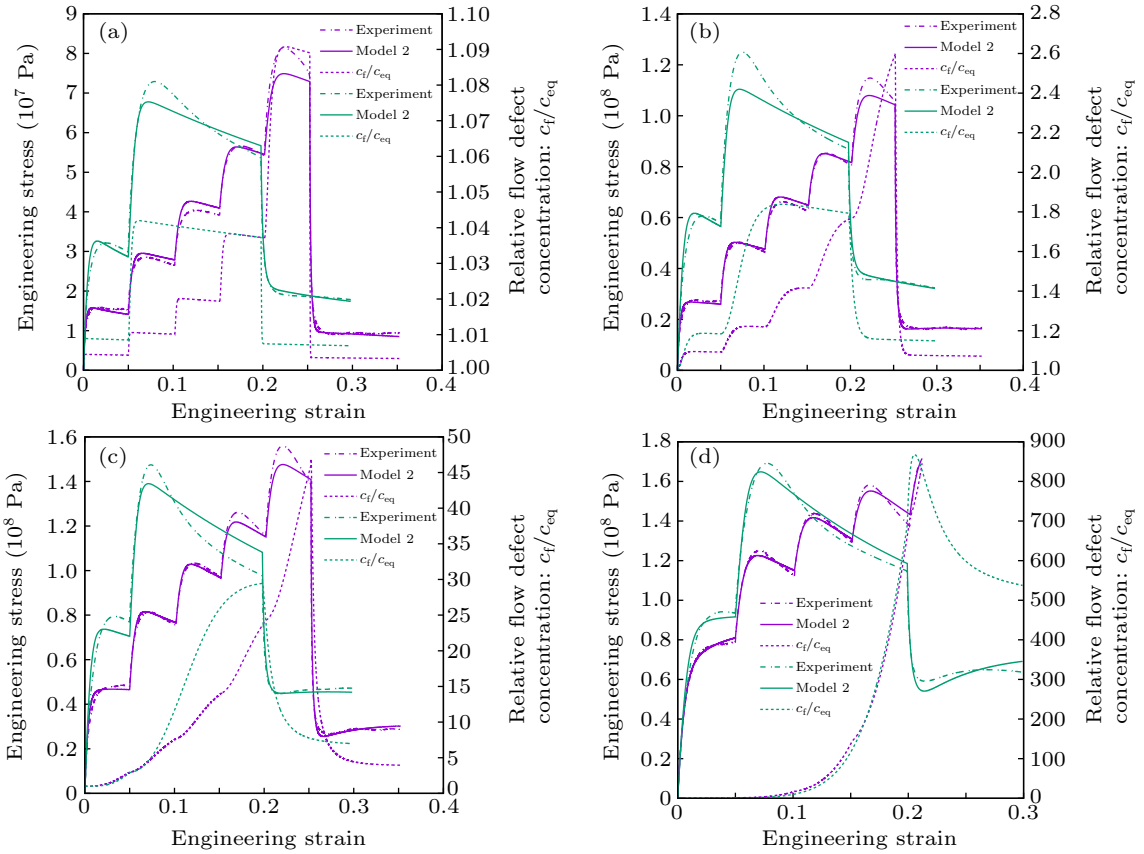


Fig. 4. Comparison of engineering stress-strain curves between experiment and optimized model 2 at (a) $T = 490$ K, (b) $T = 485$ K, (c) $T = 480$ K, and (d) $T = 475$ K. The dotted curve represents the variation of c_f/c_{eq}. All calculations were performed using true stress and true strain data and then transformed back into engineering stress and engineering strain for plotting.

A few points must be emphasized here for certain parameters.

(i) E: DMA experiments conducted in tension provide values of the storage modulus, E', which can be compared with those obtained here. The measured values are $E'(475) = 16$ GPa, $E'(480) = 15.6$ GPa, $E'(485) = 14.9$ GPa, and $E'(490) = 13.8$ GPa. These differ significantly from the values obtained from the model, and the discrepancy tends to increase with temperature. Additionally, the very initial slopes of the stress–strain tensile curves lead to rather scattered estimates of E, which are close to those obtained by DMA: $E(475) = 12.8$ GPa, $E(480) = 15$ GPa, $E(485) = 14.3$ GPa, and $E(490) = 18.7$ GPa. All this suggests that, in model 2, E reflects not only elastic deformation but also part of the inelastic deformation, since the latter is absent from the model.

(ii) $\dot{\varepsilon}_{0,c}$: In the FVM, this parameter is given by $\dot{\varepsilon}_{0,c} = 2\nu_D \exp(-\Delta G^m/kT)$, as already mentioned, which is an increasing function of T. However, the fitted values decrease significantly as temperature increases, corresponding to a negative activation energy. This term evolves in opposition to $\dot{\varepsilon}_0$, which is supposedly $c_f\dot{\varepsilon}_{0,c}$ in the FVM framework. When calculating $c_{eq} \times \dot{\varepsilon}_{0,c}$, the resulting values are close to $\dot{\varepsilon}_0$ obtained by fitting relation (Eq. 3). Hence, the evolutions of c_{eq} and $\dot{\varepsilon}_{0,c}$ compensate one another.

(iii) V: The activation volume increases with temperature. Its variation is more monotonic than that obtained above by fitting relation Eq. 3, and the values are higher than those found through Eq. (3) (compare Tables 1 and 4). Its increase appears to start around $T = 480$ K, near the glass transition temperature of 478 K. This may suggest an increase in cooperativity within this temperature range.

(iv) a_x decreases as temperature increases, suggesting less

efficient—or less necessary—free volume creation at higher temperatures.

(v) k_r exhibits an evolution similar to that of $\dot{\varepsilon}_{0,c}$, decreasing with increasing temperature. This trend is unusual for a parameter expected to be thermally activated, as reported for instance in $Pd_{40}Ni_{40}P_{20}$ MGs.[52]

(vi) c_{eq}: The flow-defect concentrations found here are of typical magnitude for MGs in the homogeneous domain. However, when compared with crystalline materials in their creep regime (see for instance Refs. [53,54]), much higher concentrations of vacancies (typically more than 10 orders of magnitude higher) are required to produce similar strain rates. This strongly questions the physical interpretation of "flow defects" as individual, more or less point-like defects with a meaningful concentration. Instead, it suggests that free volume, however efficient, should be interpreted differently, possibly as emerging from a mechanism completely unrelated to preexisting uncorrelated defects, a picture often used to interpret the free volume model.

Figure 4 also shows that the flow-defect concentration varies more at lower temperature relative to the equilibrium flow-defect concentration: it reaches nearly $900c_{eq}$ at $T = 475$ K and less than $1.1c_{eq}$ under the same mechanical conditions at $T = 490$ K. This is due to the fact that c_{eq} decreases faster than a_x/k_r as T decreases. Thus, the relative importance of dynamically created flow defects becomes higher at lower temperature relative to the static equilibrium flow-defect concentration (see Eq. (13)).

Considering the overall fit quality (see Fig. 4), it is never possible to satisfactorily reproduce the stress overshoots in strain and/or stress amplitude, whether in the 3- or 6-sequence experiments, indicating a significant failure of model 2 in this respect. This unsatisfactory fit quality may be interpreted in two ways: (i) it could reflect a significant difference between the mechanical behaviour of this glass and that of others (such as $Zr_{52.5}Al_{10}Cu_{27}Ti_{2.5}Ni_8$, tested at $T = T_g$,[17] or $Pd_{40}Ni_{40}P_{20}$, tested at $T = 0.93T_g$[41]), for which model 2 can satisfactorily rationalize stress–strain curves under similar conditions; or (ii) it may indicate that the FV model—here in the form of model 2—is insufficient to describe the mechanical behaviour in transient regimes preceding steady states. The latter explanation appears highly likely, without excluding the former, since the FVM does not account for inelastic deformation—let alone any distribution of relaxation times or activation energies as observed in MGs.[55–58] Hence, the emerging picture is that the FVM can rationalize MG rheology in steady states and partially capture transient states such as stress overshoots and undershoots, but only by absorbing anelastic effects into the elastic modulus, which is physically unsatisfactory, as these effects are crucial for MGs in the homogeneous regime. The free volume model thus serves as a useful phenomenological tool but lacks a clear physical foundation and does not account for viscoelastic deformation. Nevertheless, the negative activation energies found here suggest that the studied HEMG behaves significantly differently from other MGs, as hinted by the FVM analysis, highlighting its value as a phenomenological tool.

6. Conclusion

In summary, we have studied the rheology of a HEMG in the homogeneous domain and analyzed its behaviour within the framework of the free volume model. Two formulations of free volume creation by deformation were considered. The first, initially proposed by Spaepen, was applied to steady-state results and leads to negative parameters, indicating the physical inconsistency of this model in the homogeneous domain and calling into question its use for modeling localization phenomena in MGs. Another formulation, based on Sietsma *et al.*'s work,[15] performs better when compared with experimental results. It was applied via an elasto-viscoplastic model but still has limitations: it does not properly capture some stress overshoots, and unphysically low values of the Young's modulus must be used, highlighting the need to account for viscoelastic effects in constitutive laws modeling the mechanical behavior of MGs at high temperature. Future work should prioritize constitutive models that explicitly decouple elastic, anelastic, and viscoplastic responses. At the same time, some fitted parameters (k_r and $\dot{\varepsilon}_{0,c}$) show negative activation energies, which is unusual and suggests that HEMGs may behave in a somewhat exotic manner compared with other, more "classic" MGs. The observed discrepancies indicate that homogeneous flow kinetics in this HEMG may differ significantly from conventional MGs, potentially requiring modifications to standard theoretical frameworks.

Acknowledgments

This project was supported by the National Natural Science Foundation of China (Grant Nos. 52271153 and 12472069) and the Natural Science Basic Research Plan for Distinguished Young Scholars in Shaanxi Province (Grant No. 2021JC-12).

References

[1] Hufnagel T, Schuh C and Falk M 2016 *Acta Mater.* **109** 375
[2] Trexler M and Thadhani N 2010 *Prog. Mater. Sci.* **55** 759
[3] Schuh C, Hufnagel T and Ramamurty U 2007 *Acta Mater.* **55** 4067
[4] Qiao J, Wang Q, Pelletier J, Kato H, Casalini R, Crespo D, Pineda E, Yao Y and Yang Y 2019 *Prog. Mater. Sci.* **104** 250
[5] Wang W 2019 *Prog. Mater. Sci.* **106** 100561
[6] Wang Y, Liu J, Jiang J and Cai W 2024 *Nat. Commun.* **15** 171
[7] Şopu D, Stukowski A, Stoica M and Scudino S 2017 *Phys. Rev. Lett.* **119** 195503
[8] Cheng Y T, Hao Q, Pelletier J M, Pineda E and Qiao J C 2021 *Int. J. Plast.* **146** 103107

[9] Cohen M and Turnbull D 1959 *J. Chem. Phys.* **31** 1164
[10] Cohen M and Turnbull D 1961 *J. Chem. Phys.* **34** 120
[11] Taub A and Spaepen F 1980 *Acta Metall.* **28** 1781
[12] Spaepen F 1977 *Acta Metall.* **25** 407
[13] De Hey P, Sietsma J and Van Den Beukel A 1998 *Acta Mater.* **46** 5873
[14] van Aken B, de Hey P and Sietsma J 2000 *Mater. Sci. Eng. A* **278** 247
[15] Sietsma J and Thijsse B J 1995 *Phys. Rev. B* **52** 3248
[16] Bletry M, Guyot P, Blandin J and Soubeyroux J 2006 *Acta Mater.* **54** 1257
[17] Bletry M, Bréchet Y, Guyot P, Blandin J and Soubeyroux J 2007 *Acta Mater.* **55** 6331
[18] Gao Y F, Yang B and Nieh T G 2007 *Acta Mater.* **55** 2319
[19] Anand L and Su C 2007 *Acta Mater.* **55** 3735
[20] Zhang H, Wang Z, Yang H J, Shi X H, Liaw P K and Qiao J W 2023 *Scr. Mater.* **222** 115047
[21] Zhu W, Liu J, Mao S and Wei X 2021 *J. Mech. Phys. Solids* **146** 104216
[22] Stolpe M, Kruzic J J and Busch R 2014 *Acta Mater.* **64** 231
[23] Lee S, Han G, Marimuthu K P and Lee H 2024 *J. Non-Cryst. Solids* **624** 122695
[24] Huang B, Tang X C, Geng C, He Q F, Yi J, Wang Q, Huang W X, Yuan Q X, Yang Y, Wang G and Wang W H 2023 *Mater. Sci. Eng. A* **869** 144726
[25] Chen S, Xu D, Zhang X, Chen X, Liu Y, Liang T, Yin Z, Jiang S, Yang K, Zeng J, Lou H, Zeng Z and Zeng Q 2022 *Phys. Rev. B* **105** 144201
[26] Zhu F, Song S, Reddy K M, Hirata A and Chen M 2018 *Nat. Commun.* **9** 3965
[27] Ge J, Luo P, Wu Z, Zhang W, Liu S, Lan S, Almer J D, Ren Y, Wang X L and Wang W 2023 *Mater. Res. Lett.* **11** 547
[28] Duan Y J, Nabahat M, Tong Y, Ortiz-Membrado L, Jiménez-Piqué E, Zhao K, Wang Y J, Yang Y, Wada T, Kato H, Pelletier J M, Qiao J C and Pineda E 2024 *Phys. Rev. Lett.* **132** 056101
[29] Song J, Zhu W and Wei X 2021 *Int. J. Mech. Sci.* **204** 106570
[30] Jiang W and Zhang B 2020 *J. Appl. Phys.* **127** 115104
[31] Xing G, Hao Q, Zhu F, Wang Y J, Yang Y, Kato H, Pineda E, Lan S and Qiao J 2024 *Sci. China Phys. Mech. Astron.* **67** 256111
[32] Mauro J C, Yue Y, Ellison A J, Gupta P K and Allan D C 2009 *Proc. Natl. Acad. Sci. USA* **106** 19780
[33] Gallino I 2017 *Entropy* **19** 483
[34] Sarac B and Eckert J 2022 *Prog. Mater. Sci.* **127** 100941
[35] Kauzmann W 1941 *Trans. Am. Inst. Min. Metall. Eng.* **143** 57
[36] Argon A 1979 *Acta Metall.* **27** 47
[37] Zhu A, Shiflet G J and Poon S J 2010 *Phys. Rev. B* **81** 224209
[38] van den Beukel A and Sietsma J 1990 *Philos. Mag. B* **61** 539
[39] Tsao S and Spaepen F 1985 *Acta Metall.* **33** 881
[40] Hao Q, Lyu G J, Pineda E, Pelletier J M, Wang Y J, Yang Y and Qiao J C 2024 *Int. J. Plast.* **175** 103926
[41] Bletry M, Thai M T, Champion Y, Perrière L and Ochin P 2014 *C. R. Méc.* **342** 311
[42] Huang R, Suo Z, Prevost J H and Nix W D 2002 *J. Mech. Phys. Solids* **50** 1011
[43] Gao Y F 2006 *Model. Simul. Mater. Sci. Eng.* **14** 1329
[44] Jiang M Q and Dai L H 2009 *J. Mech. Phys. Solids* **57** 1267
[45] Li J C, Wei Q, Chen X W and Huang F L 2014 *Mater. Sci. Eng. A* **610** 91
[46] Lu J, Ravichandran G and Johnson W L 2003 *Acta Mater.* **51** 3429
[47] Hindmarsh A C, Brown P N, Grant K E, Lee S L, Serban R, Shumaker D E and Woodward C S 2005 *ACM Trans. Math. Softw.* **31** 363
[48] Wächter A and Biegler L T 2006 *Math. Program.* **106** 25
[49] Scilab Team 2024 *Scilab: Open source software for numerical computation Computer Software*
[50] Squire W and Trapp G 1998 *SIAM Rev.* **40** 110
[51] Ljung L 1998 *System Identification in Signal Analysis and Prediction* (Boston, MA: Birkhäuser Boston) pp. 163–173
[52] Duine P A, Sietsma J and Van den Beukel A 1992 *Acta Metall. Mater.* **40** 743
[53] Kassner M E 2015 *Fundamentals of Creep in Metals and Alloys* (Third Edition) (Butterworth-Heinemann)
[54] Gottstein G 2004 *Physical Foundations of Materials Science* (Springer)
[55] Lee K S, Eckert J and Chang Y W 2007 *J. Non-Cryst. Solids* **353** 2515
[56] Jiao W, Wen P, Peng H L, Bai H Y, Sun B A and Wang W H 2013 *Appl. Phys. Lett.* **102** 101903
[57] Duan Y J, Zhang L T, Wada T, Kato H, Pineda E, Crespo D, Pelletier J M and Qiao J C 2022 *J. Mater. Sci. Technol.* **107** 82
[58] Cui J B, Lyu G J, Hao Q, Zhu F, Khonik V A, Duan Y J, Wada T, Kato H and Qiao J C 2024 *Mech. Mater.* **196** 105078